VTT Technical Research Centre of Finland

Phase diagrams with the driving force and extent of reaction as axis variables

Koukkari, Pertti; Pajarre, Risto

Published in:
Calphad: Computer Coupling of Phase Diagrams and Thermochemistry

DOI:
10.1016/j.calphad.2021.102290

Published: 01/09/2021

CALPHAD: Computer Coupling of Phase Diagrams and Thermochemistry 74 (2021) 102290

Contents lists available at ScienceDirect

Calphad

journal homepage: www.elsevier.com/locate/calphad

Phase diagrams with the driving force and extent of reaction as axis variables

Pertti Koukkari *, Risto Pajarre

VTT Technical Research Centre of Finland, P.O. Box 1000, FI-02044, Finland

ARTICLE INFO

Keywords:
Driving force
Affinity
Extent of reaction (EOR)
Axis variables. phase diagrams
Partial equilibria

ABSTRACT

A method where a conjugate pair of the driving force (affinity, D) and extent of reaction (EOR, ξ) are used as axis variables to present non-equilibrium conditions of multiphase systems as Calphadian phase diagrams is introduced. Three examples for various thermochemical systems include a solid state reaction, steel melt solidification and an aqueous sorption-precipitation system. Both equilibrium and non-equilibrium diagrams were produced to study the thermodynamic validity of the suggested technique. The use of D, ξ variables can be applied in typical Gibbs energy minimizing programs and provides additional degrees of freedom in the diagrammatic analysis of various multiphase problems.

1. Introduction

For non-equilibrium systems with internal entropy producing processes the combined first and second law of thermodynamics as introduced by Hillert and e.g. by Liu & Wang includes the driving force (D) as an intensive state variable, in conjunction with the advancement of the internal change (ξ), which is then the respective extensive property [1,2]. As for systems with chemical reactions, the terms Affinity and Extent of Reaction are customarily used, such as they were introduced by De Donder [3]. While both Hillert and Liu & Wang insinuate that there is a possibility of utilising the correspondence of equilibrium properties as applied in traditional equilibrium phase diagrams and then D and ξ in non-equilibrium ('frozen-in') systems, an appropriate methodology for this has not been presented. On the other hand, in the Constrained Gibbs Free energy minimization (CFE) method by Koukkari and Pajarre [4,5] the conjugate pair of D, ξ appears as one key concept for the calculation procedure. In the non-equilibrium applications of the CFE method the driving force may be either given as an input condition or is received as the non-equilibrium 'constraint potential' – i.e. the affinity of the internal chemical change – as the result of the calculation. The advancement of the internal process is then either given as an external constraint, being an independent variable of the non-equilibrium system or becomes defined from the internal conditions of a metastable state and acts as a dependent variable of the system. Then, it is obvious that these features of the CFE method together with the conjugate properties D and ξ can be used to construct phase diagrams for such systems, where partial equilibria exist during a relatively slow chemical or phase change.

1.1. General theory

Following Hillert, there is for the energy, entropy and volume scheme:

$$dU = TdS - PdV + \sum \mu_j dN_j - Dd\xi \tag{1}$$

$$-dS = -\left(\frac{1}{T}\right)dU - \left(\frac{P}{T}\right)dV + \sum \left(\frac{\mu_j}{T}\right)dN_j - \left(\frac{D}{T}\right)d\xi \tag{2}$$

$$dV = \left(\frac{T}{P}\right)dS - \left(\frac{1}{P}\right)dU + \sum \left(\frac{\mu_j}{P}\right)dN_j - \left(\frac{D}{P}\right)d\xi \tag{3}$$

where N_j refers to the amounts of components in the thermodynamic system. The respective conjugate pair variables then become as listed in Table 1.where $-D$ and ξ are also regarded as a pair of conjugate properties, $-D$ being a potential, which is obtained as

$$-D = \left(\frac{\partial U}{\partial \xi}\right)_X \tag{4}$$

where X represents all conjugate variables in equation (1). The extent of reaction is then regarded as an independent variable and the respective conjugate potentials are defined for the frozen-in state (Hillert p 22-23).

* Corresponding author.
E-mail address: pertti.koukkari@vtt.fi (P. Koukkari).

https://doi.org/10.1016/j.calphad.2021.102290
Received 4 August 2020; Received in revised form 29 March 2021; Accepted 30 March 2021
Available online 18 June 2021

Table 1
Characteristic sets of conjugate pairs of state variables.

U	T,S	$-P,V$	μ_j,N_j	$-D,\ \xi$
$-S$	$-1/T,U$	$-P/T,V$	$(\mu_j/T),N_j$	$-D/T,\ \xi$
V	$T/P,S$	$-1/P,U$	$(\mu_j/P),N_j$	$-D/P,\ \xi$

The Gibbs energy is then respectively

$$dG = -SdT + VdP + \sum \mu_j dN_j - Dd\xi \tag{5}$$

In equations (1), (2) and (5) the last term $Dd\xi$ drops off at equilibrium ($D = 0$) and ξ is a dependent variable of the system, determined by the equilibrium conditions and mass balance. With $d\xi = 0$ and $D > 0$ the system is under a constrained state or 'frozen-in-condition' and ξ remains an independent variable (Liu & Wang, p 4-5). The natural variables of Gibbs energy then become T, P, N_j and ξ (Liu 2020, [6]).

1.2. Chemical reactions in a closed system

For chemical changes or respective phase transformations in a closed system one can distinguish a specific case where the constraints are set for selected non-equilibrium reactions. When the internal reaction constraints are given, a free energy minimization can be performed and the *min*(G) calculation can be used to provide the composition and state properties of the 'frozen-in' system at given conditions defined by the mass balance, T, P and ξ .

To incorporate extent of chemical reactions as a constraint into *min*(G) calculations a technique analogous with the conventional mass balance constraints will be applied. A general condition for *min*(G) problems is the conservation of the amount of independent system components N_j:

$$N_j = N_j^\circ \quad ; j = 1, \ldots NC \tag{6}$$

The amounts of components (initially N_j°) are connected with the amounts of chemical constituents n_k via the stoichiometric conservation matrix, the elements of which are denoted as c_{kj}:

$$N_j = \sum_{k=1}^{N} c_{kj} n_k \tag{7}$$

Similarly, using massless reaction constraints for extents of reaction (ξ_r) there is

$$\xi_r = \xi_r^t \ ; \ r = 1, \ldots NR \tag{8}$$

where superscript t relates to incremental time and subscript r to each reaction (total number of reactions is NR). The extent of a chemical reaction obviously is deduced from the molar amounts of constituents participating in each reaction. Thus:

$$\xi_r = \sum_{k=1}^{N} c_{kr} n_{kr} \tag{9}$$

While T, P and $N_J$in equation (5) as external variables can be controlled from outside the system, the advancement of the chemical reactions ξ_r is an internal variable. However, under the given restriction ($\xi_r = \xi_r^t$), it can be treated as an external variable (see Hillert, p 4). The constraints related to the advancement of the internal processes are then incorporated into the conservation matrix of the Gibbs'ian system. In terms of massless (virtual) system components and respective virtual phases, the input amount of the latter defining the given ξ_r^t in a sequential calculation. When the ξ_r -constraint is set, the minimization of the free energy function at constant T, P,N_J and given ξ_r provides a method to calculate nonequilibrium state properties for this intermediate state as a local equilibrium. In a former study e.g. the paraequilibrium solidification system was regarded as a kind of local equilibrium (Hillert, p 312), and the constraints were deduced from the given ratio of substitutional components in the mother phase and defined along this ratio as virtual components affecting each stoichiometric phase that may appear stable in the Gibbs'ian calculation (Pelton et al. [7]). For systems with chemical reactions, the reaction matrix is transformed into an enlarged conservation matrix that includes both mass balance and reaction constraints, where the latter apply to explicit (kinetically slow) reactions. The driving force is inherently solved by the Gibbs'ian procedure as the chemical potential of the introduced virtual component, typically assigned for a single slow reaction.

Using the Lagrange method of undetermined multipliers, the objective function to be minimized includes, in addition to the NC conventional mass balance constraints (equations (6) and (7)), the NR new constraints (equations (8) and (9)) as follows:

$$L = G - \sum_{j=1}^{NC} \lambda_j \left(N_j - N_j^\circ \right) + \sum_{j=NC+1}^{NC+NR} \lambda_j \left(\xi_r - \xi_r^t \right) \tag{10}$$

The solution gives the chemical potentials of the system components in terms of the Lagrange multipliers

$$\lambda_j = \left(\frac{\partial G}{\partial N_j} \right) \equiv \mu_j \ ; \quad j = 1, \ldots NC \ ; \ \left(T, P, \ N_{i \neq j}, \xi_r \text{ constant} \right) \tag{11}$$

in analogy with the definition of the component potentials, one obtains then:

$$\lambda_j = \left(\frac{\partial G}{\partial \xi_r} \right) \equiv -A_r \ ; \quad j = NC + 1, \ldots NC + NR; \left(T, P, \ N_j \text{ constant} \right) \tag{12}$$

where $A_r = D_r$ is the affinity (driving force) of each constrained reaction in the system. Note that from (10) and (12) it is obvious that each reaction constraint represents another massless component in the Gibbs'ian system and thus subscripts j and r could formally be replaced by one index symbol (Pajarre et al. [5]). It is yet often practical to distinguish between the two entities and follow the number of components and reactions separately.

With the said reaction constraints incorporated into phase diagram software, such as FactSage [8], the corresponding diagrams for non-equilibrium conditions can be produced in terms of D and ξ. The conjugate properties applicable for potential diagrams listed in Table 1 indicate that the driving force is then equivalently comparable with the component potentials (μ_j). As for molar phase diagrams, the conditions analogous to conventional equilibrium phase diagrams apply. Non-equilibrium affinity ($D = A_r$) will appear as a potential, and ξ as an extensive variable that must be related to some other quantity. The latter condition is in conformance with the conventional tradition of chemical reaction kinetics, where a proportional figure ($0 \leq \xi \leq 1$) for the advancement of a given reaction is commonly used, typically representing the fraction of a reactant consumed. Using such premises, examples of diagrams constructed for some non-equilibrium reactive systems are introduced below.

The virtual components and virtual phases have been used in, e.g. ChemSheet software for quite some time [9,10], yet the technique is generally applicable for such thermodynamic software that makes use of the Lagrange method. The properties of these massless components when constraining the extent of chemical reactions in Gibbs energy minimization are collected in the Supplementary Appendix. The min(G) algorithm for ChemSheet is provided by the well-known ChemApp library by Eriksson [11], in which it is possible to use arbitrary names for both the virtual components and phases. However, in FactSage, which was here used for calculating and drawing the phase diagrams, such freedom in its nomenclature is currently not available. This technical

problem was circumvented by using the symbols of chemically inert elements (such as noble metals of gases) for the virtual components with the input data files prepared originally for ChemSheet. The symbols r_i for phases and v_j for components were, however, used in the matrix formulae and in the graphs that were produced. Reactions (R_i) were indexed as 1,2 and used repeatedly for each case for both r_i and v_j as there should be no grounds for confusion.

2. Example of a solid state reaction: titania calcination

The first example presents the formation of titanium dioxide in a calciner, which is one of the final stages of the titania pigment making sulphate process. The feed consists of wet titanium oxyhydrate slurry with sulphuric acid and titanium sulphate residues. The chemical compounds of the mix are approximated as titanium oxyhydrate and -oxysulphate, $TiO(OH)_2$ and $TiOSO_4$. During calcination, the slurry is dried and finally the hydrate decomposes, leaving the product titanium dioxide in the bed. From the oxyhydrate, at relatively low temperatures (ca. 200 °C) the crystalline form anatase, $TiO_2(An)$, is formed first, and only in the high temperature zone of the furnace end, the thermodynamically stable rutile form $TiO_2(Ru)$ appears as the desired product. The reactions are as follows:

$$TiO(OH)_2 + TiOSO_4 \leftrightarrow TiO_2\ (An) + gas$$

$$TiO_2\ (An) \rightarrow TiO_2\ (Ru)$$

The phase transformation of anatase to rutile is commonly recognised as a slow reaction with high activation energy, while the calcination reactions of oxyhydrate and oxysulphate occur at lower temperatures with moderate rates and in the process simulation of the calcination furnace they are typically considered as equilibrium reactions. This approach is also confirmed by long-term practical experience from the titania industry (see Dumont and Belanger, Ketonen et al., Ginsberg & Modigell [12–14]). With such an assumption, the conditions of local chemical equilibria can be illustrated by using the driving force and extent of the anatase to rutile transformation reaction, for which the massless constraint has been set [15].

The technique used for introducing constraints for the extent of reactions into the Calphadian Gibbs energy minimizer has been extensively described in earlier work [4,15–21] and is only briefly discussed here. The constraints are formed from corresponding pairs of virtual components and phases, representing the forward and reverse reactions respectively. The virtual phases serve for the introduction of the advancement of the desired reaction, while the connection with the respective massless component allows for the conservation of the actual species (reactant or product), following the same reaction kinetics. More than one species can be involved and the corresponding matrix elements are defined by the actual stoichiometry of the constrained reaction(s).

The extended matrix for the simple calcination system is shown as an example in Table 2. The conventional stoichiometry has been extended to include the constituent-component pairs for the forward and reverse constrained reaction, in this case the anatase to rutile transformation. In a sequential Gibbs'ian calculation the extent of reaction must be given as input of either r_i^+ or r_i^- (in moles) and the solution in each sequence will result in the affinity (driving force) of the reaction as the chemical potential of the virtual component v_j. As the virtual phases are introduced with zero standard chemical potential ($\mu^0_{r_i^\pm} \equiv 0$), the affinity is also received from the corresponding activity of the virtual phase r_i^+ or r_i^-.

Table 2
Extended matrix for the titania calcination system.
Constraints set for the reaction $TiO_2(An) \rightarrow TiO_2(Ru)$; (r_1^+, r_1^-)

O	H	S	Ti	v_1	
2	0	0	0	0	O_2(g)
2	0	1	0	0	SO_2(g)
3	0	1	0	0	SO_3(g)
1	2	0	0	0	H_2O(g)
3	2	0	1	0	$TiO(OH)_2$
5	0	1	1	0	$TiOSO_4$
2	0	0	1	0	TiO_2(An)
2	0	0	1	1	TiO_2(Ru)
0	0	0	0	1	(r_1^+)
0	0	0	0	-1	(r_1^-)

The set of Table 2 has been successfully used for practical calcination studies as well as for process simulation and scale-up [13,15]. Here, the approach is used as an example to introduce the extended matrix method for phase diagram studies. As the phase diagrams in this work were produced using FactSage, the technique had to be adapted to conform to the present software requirements. Then, only one virtual phase (the one for forward reaction) could be applied, as for neutral (non-ionic) constituents only positive matrix elements are allowed. However, the 1-directional approach is also fully sufficient in this case. The system then has an additional component (5 instead of 4 in the respective global equilibrium system) and one additional phase, both of which are included as variables in the phase diagram calculation. Then the conventional rules of phase diagram calculations are applied, that is, one may choose n potentials for the diagrams ($n < NC + 1$) and form $NC + 1 - n$ ratios out of the non-corresponding extensive variables and then use two of the $NC + 1$ variables as independent xy-coordinates and hold the others constant. As stated above, the affinity can be chosen as one of the potentials and the extent of reaction as one of the extensive variables and both may also be used as diagram axes.

To illustrate the system of our first example in Fig. 1 the global equilibrium system is presented as T, H_2O/TiO_2 -diagram using the molar ratio 0.2 for $TiOSO_4/TiO_2$. Heating leads to decomposition of the oxyhydrate at ca. 200 °C and then, while the calcination proceeds the oxysulphate is also decomposed between 600 and 700 °C. Rutile is, however, the stable TiO_2 phase throughout the temperature range, becoming even more stable at lower temperatures as is shown by the isoactivities of anatase. Yet, heating of the mixture first leads to anatase-TiO_2, and formation of the desired end product, rutile, only takes place in elevated temperatures above 900 °C [13,22]. In Fig. 2 this effect is shown in terms of the T,ξ-diagram.

Fig. 2 shows the respective stability ranges as presented in the equilibrium diagram of Fig. 1, however, as rutile formation is constrained, anatase- TiO_2 is also present in the respective phase fields when $\xi<1$. In the lower right hand corner a barred field emerges, where the virtual r_1^+ phase appears as 'stable' – this region is due to equilibrium of $TiOSO_4$ with rutile-TiO_2 in this temperature range, preventing any formation of rutile with $\xi>0.8$ until the mixture is heated to such temperature where the oxysulphate decomposes. The area that shows the 'presence' of the virtual phase does not have a physical meaning and appears as barred. The limiting zero phase fraction line indicates the thermodynamic limit of any phase composition in terms of the extent of reaction and temperature. While no kinetic data is required to produce the T,ξ-diagram, it should be of interest to trace an actual reaction path within its sections. A kinetic model giving an extent of reaction in terms of T could be included to illustrate a reaction path but should, of course, be based on experiment. As a show case, a few $T(\xi)$ -curves have been superimposed onto the phase diagram in scale. The curves have been deduced from the kinetic data of MacKenzie in Table 3 [22], using 1 and 10 h residence times for selected anatase-rutile conversions as parameters. The $T(\xi)$ -inserts here serve merely as a schematic illustration without quantitative substantiation (MacKenzie only made experiments with anatase-rutile mixtures), yet their position points out the temperature dependency of the (bulk) rutile formation and also elucidates the possible use of T,ξ-diagrams in any similar context.

The predominance of anatase as the first reaction product of the calcination process may be explained by the surface energy effect of the formed titania particulates, see, e.g. Mauer et al. [23]. While the surface energy is part of the Gibbs energy of formation of both phases, for small

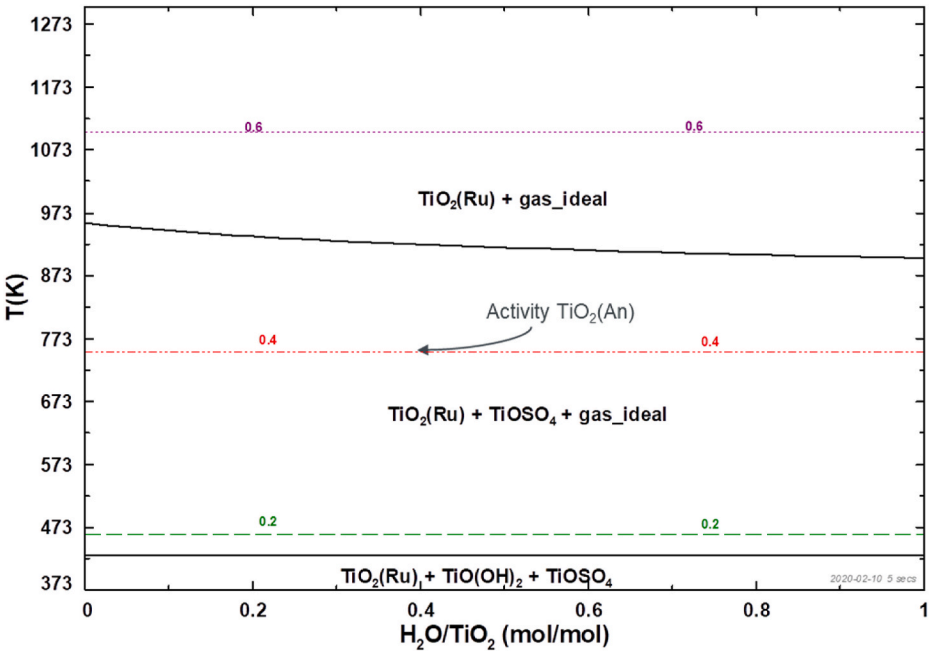

Fig. 1. Equilibrium phase diagram of the titania calcination system TiO_2- $TiOSO_4$- H_2O at 1 atm. Molar ratio $TiOSO_4/TiO_2$ =0.2; $TiO_2(An)$ activities also shown.

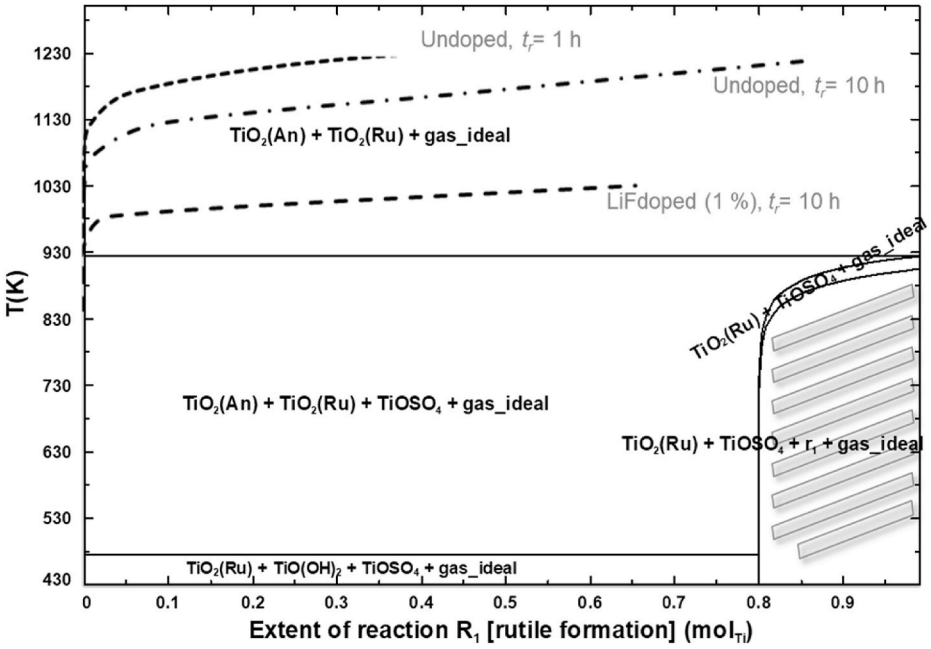

Fig. 2. T,ξ-phase diagram of the $Ti-O-H-S-v_1$-system at 1 atm. Molar ratios O/Ti =3.4, H/Ti =1.6, S/Ti =0.2. Solid lines indicate equilibrium phase boundaries. The striped area with stable r_1-phase exceeds the equilibrium limit of $TiO_2(Ru)$ and $TiOSO_4$, when $\xi > 0.8$. The superimposed dotted and dash-dotted lines indicate measured anatase to rutile transformation kinetics according to the data of MacKenzie [22] at given residence times.

Table 3
Reaction kinetics of anatase-rutile transformation (MacKenzie 1975).

Rate law (EOR rutilization vs. time)	$\xi = 1-(1-k*t)^3$	
Rate constant k (h^{-1})	$k = A*\exp\left(\frac{-E_a}{RT}\right)$	
Type of catalyst	none	LiF (1 %)
Arrhenius factor A (h^{-1})	1.80E+17	7.56E+29
Activation Energy E_a($kJ*mol^{-1}$)	441.99	642.293

particulates there appears a temperature range where the ΔG_f°-values for nano-scale anatase and rutile become equal and anatase eventually appears more stable. Following this observation, the phenomena can be illustrated by using T,D-diagrams, in which the affinity of the rutile forming reaction has been used as x-axis (note that $\mu^0_{r_1^\pm} \equiv 0$ and the affinity of the reaction is thus received in terms the activity of the virtual phase $r_1^\pm$.

The use of the virtual conjugate pair thence allows for viewing the relative activities of anatase and rutile of equal stoichiometry in a single diagram, as shown in Fig. 3. While the T,D-diagram is a typical potential

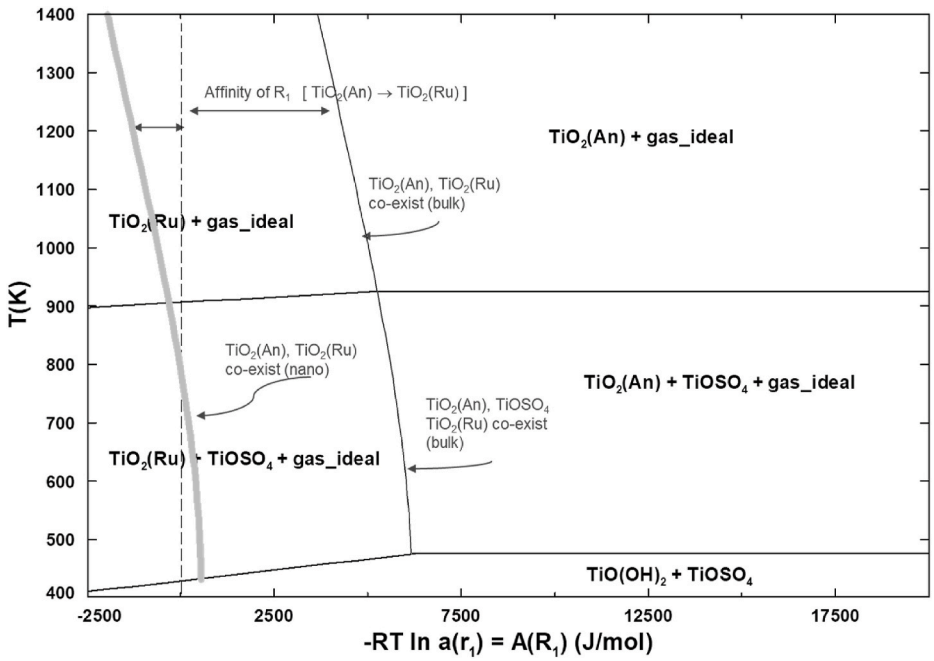

Fig. 3. T,D-diagram for the $Ti-O-H-S-v_1$ -system; molar ratios O/Ti =3.4, H/Ti =1.6, S/Ti =0.2, 1 atm. x-axis gives the affinity of the reaction (R_1) calculated in terms of the activity of the virtual phase r_1. Sections are divided by equilibrium co-existence lines. The softened grey curve represents anatase-rutile co-existence at average particle spherical diameter φ ~15 nm (Mauer et al. 2013 [23]). As for the superimposition used see text.

diagram, instead of zero phase fraction lines the co-existence limits are shown. Then the temperature dependent affinity of anatase-to-rutile formation is the distance from the $TiO_2(An)-TiO_2(Ru)$ coexistence line to the dotted line of $D=0$. The softened grey co-existence line for $TiO_2(An)-TiO_2(Ru)$ was calculated by setting the enthalpies of formation of anatase and rutile to correspond to the ΔG_f° -values (in our system) published by Mauer et al. for particulates of 15 nm diameter. The two diagrams were then combined by using the superimposing technique of FactSage to show the surface energy effect in one illustration. For more extensive and exact work regarding the particulate size, a refined database for surface energies should of course be available.

3. Formation of calcium-aluminate inclusions in steel solidification

Aluminium-deoxidizing during ladle treatment is a common practice in steel manufacturing. Following such treatment, the steel will contain non-metallic inclusion phases that will have effects on grain refining and machinability of the final product. To control the inclusion composition, as well as their shape and size, calcium is added to the solidifying melt [24]. After calcium treatment, mainly *Ca*-aluminates are formed as inclusions while sulphur is also captured as solid *CaS*. An additional benefit of the *Ca* treatment is that *Ca* addition transforms solid alumina

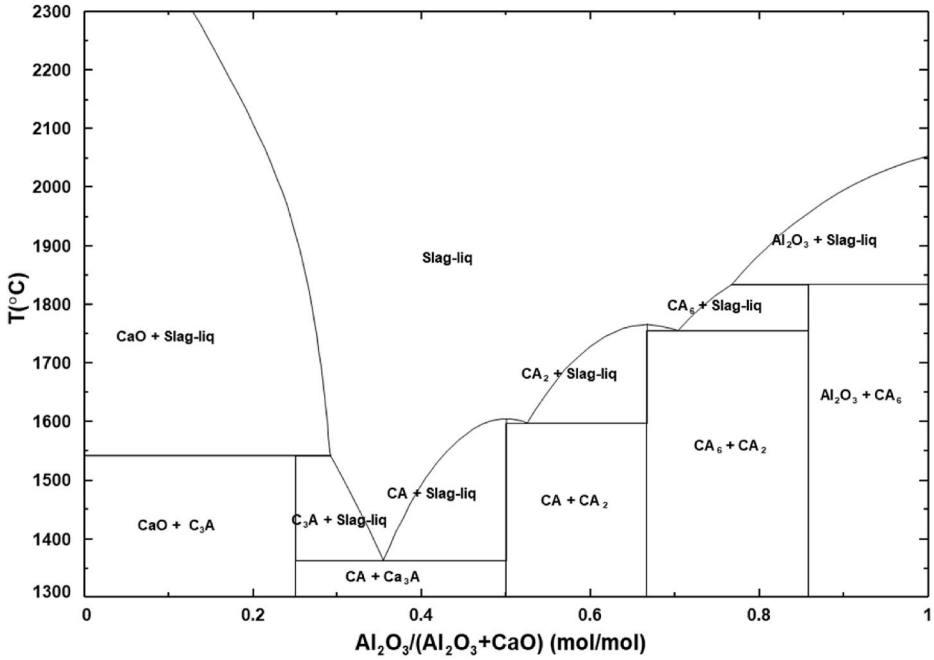

Fig. 4. Al_2O_3-CaO equilibrium phase diagram.

inclusions to liquid calcium aluminates and the risk of nozzle clogging during continuous casting can be reduced. In Fig. 4 the Al_2O_3_CaO system has been illustrated. The used abbreviations with some key properties of the *Ca*-aluminate phases as collected by Lind are given in Table 4.

The comprehensive analysis of *Ca*-aluminate and *CaS* inclusion formation published by Lind was then applied in the well-known steel solidification model by Holappa et al. [25]. In their model the partial equilibria inclusion phases were coupled with the kinetics of solidifying steel at temperatures below 1500 °C. The interdendritic solidification model (IDS) developed at Helsinki University of Technology by Miettinen et al. [26] was coupled with the ChemApp equilibrium programming library to calculate interactively and stepwise steel solidification and inclusion formation/transformation in the residual liquid fraction. In this coupled IDS-ChemApp (IDS-ICA)-model ChemApp was used to solve the multiphase equilibria of the inclusion phases, while the cooling rate of the melt was adapted from IDS [27].

In what follows, the solidification process was analysed with the CFE method to follow the respective partial equilibria of *Ca*-aluminate inclusions and the inclusion formation was further contemplated in terms of T, ξ- and T, D-diagrams.

To apply the CFE method for both the solidification model for comparison with the IDS-ICA approach and to produce the D, ξ- phase diagrams, constraints must be set for the solidifying *Fe_fcc* and *Fe_bcc* phases. As they can be in mutual equilibrium, one constraint applied for both is sufficient. Then, it is straightforward to perform calculations, where stepwise formation of solid iron takes place in given temperatures and the rest of the system, consisting of liquid slag and a number of pure substances (mainly oxides and sulphides) will be allowed for mutual equilibria. Depending upon the *O*- and *Ca*-content of the steel, one can find at a given temperature either solid aluminates, aluminate + liquid oxide, liquid oxide only, or liquid oxide + $CaS-$ precipitate in equilibrium with the liquid steel.

In Fig. 5 the solidification result with CFE has been calculated by using ChemSheet, using 0.35 % of *C*, 0.25 % *Si* and 0.25 % *S*with 20 ppm of total oxygen, 20 ppm of calcium and 200 ppm of aluminium in the feed. The feed composition as well as the solidification curve (f_{liq}, i.e. fraction of liquid vs. temperature) is adapted from the work of Holappa et al. [25,28]. The phases formed as well as their amounts comply well with the IDS -model, yet one may note that with feed amounts as indicated there is a shift of ca. 10–25° in each of the steep phase transformation points. The discrepancy is due to the two kinetic assumptions used in the IDS-ICA model: The phase transformation points are selected by the IDS model and merely the formation of inclusion phases at the shifted temperature is then calculated with ChemApp. On the other hand in the IDS-ICA model, following a modified Scheil approach, the formed inclusions are also in part removed from liquid to solid as the steel is solidifying, and the content of each element in the melt is reduced in the same ratio as the element becomes present in the inclusions [27]. The partial equilibrium model, however, gives a compliant method for analysing the types of inclusions in different compositions and temperatures and was here adapted to exemplify the D, ξ.-phase diagram approach.

Table 4
Melting point data of *Ca*-aluminates (Lind 2006 [24]).

Abbreviation	Chemical formula	CaO (wt-%)	Al2O3 (wt-%)	Melting point (°C)	Melting point FactSage (°C)
A	Al_2O_3	0	100	2050	2052
C3A	$3CaO{*}Al_2O_3$	62	38	1539	1540
CA	$CaO{*}Al_2O_3$	35	65	1590	1598
CA2	$CaO{*}2Al_2O_3$	22	78	1775	1750
CA6	$CaO{*}6Al_2O_3$	8	92	1833	1833

By choosing the extent of solidification $\xi(Fe(s))$ as the x-axis, a T, ξ-diagram for the partial equilibria in the solidification process can be constructed and is shown in Fig. 6. The composition of the system is as shown in the figure (sulphur was not included for simplicity). The open region below 1528 °C represents that of undercooled melt, which is likely to appear in the solidification process, depending on the cooling rate. In this range the iso-activity lines of the virtual phase r_1^+ are also shown. At $a(r_1^+) = 1$ the driving force of solidification is nil and the respective zero phase fraction line indicates then the $Fe(liq) - Fe(s) -$ equilibrium at each temperature. Exceeding this limit would appear thermodynamically inconsistent. The barred region may yet not be regarded as entirely non-physical, as it does correspond to the superheated solid in a reverse (melting) process.The compositions thereof can be calculated by excluding the virtual r_1^+ phase from the computational system.-

Fig. 7 shows a comparison between the T, ξ-solidification diagram (right) and respective T, D-potential diagram (left). The shaded areas represent the undercooling section of the solidification process. The equilibrium between solid and liquid iron in the potential diagram is given by the zero affinity limit in the middle. The tilted (half-diagonal) is the limit of unsolidified melt, and the affinities on its right-hand side are obviously physically irrelevant. The rectangular region to the left of zero affinity in the T, D-diagram corresponds to the 'over-solidified' area above the solid-liquid equilibrium line in T, ξ-diagram. The inclusion (*Ca*-aluminate) phases are shown in both diagrams according to their partial equilibrium stability.

4. Absorption of carbon dioxide to the aqueous sodium carbonate solution

As was earlier shown by Hack [29] and published recently in detail by Pelton et al. [30], true phase diagram sections for aqueous systems can be calculated thermodynamically with currently available software and databases. In FactSage, the aqueous phase diagrams can be calculated with various axis variables under a wide variety of constraints for real (i.e. non-ideal) solutions and for any number of components. For constant redox potential and pH respectively, iso-Eh and iso-pH lines may optionally be plotted in the diagrams. Use of an affinity-extent of reaction approach for axis variables provides an interesting technique to analyse the conditions in aqueous solutions, which often appear in near-equilibrium or metastable ('freezing-in') conditions, for which, however, e.g. temperature and pH can be measured with reasonable accuracy. To illustrate this approach, the chemistry of carbon dioxide absorption to caustic soda solution is briefly considered here in terms of the aqueous phase diagrams, presented both for equilibrium and for non-equilibrium conditions.

The immersion of carbon dioxide in solutions with elevated pH is well-known and applied for several practical purposes. Most applications deal with gas sorption to carbonate solutions of moderate concentrations in a two-phase gas-liquid systems (e.g. Cents et al., Ghosh et al. [31,32]) where precipitation of solid carbonates is avoided. The example chosen here is, however, the absorption of carbon dioxide to concentrated Na_2CO_3 solutions, applied in commercial sodium bicarbonate $NaHCO_3$ production, studied experimentally e.g. by Wylock et al., who also constructed a mechanistic reaction model to calculate time-dependent pH-development in the brine absorbing carbon dioxide at atmospheric conditions [33]. Another bulk application of the Na_2CO_3 -absorption is natural gas purification where dissolving CO_2 to a carbonate brine also allows for the simultaneous removal of acid gas impurities, typically H_2S [34]. In the latter application both the CO_2 and the H_2S impurities will remain in the brine solution, methane is recovered as a gaseous product and can be deported to further use. Gas purification is concurrently gaining new interest, characteristically for biogas cleaning. The leftover bicarbonate solution can be regenerated (to produce pure CO_2) and recycled in such a process. The capacity of the

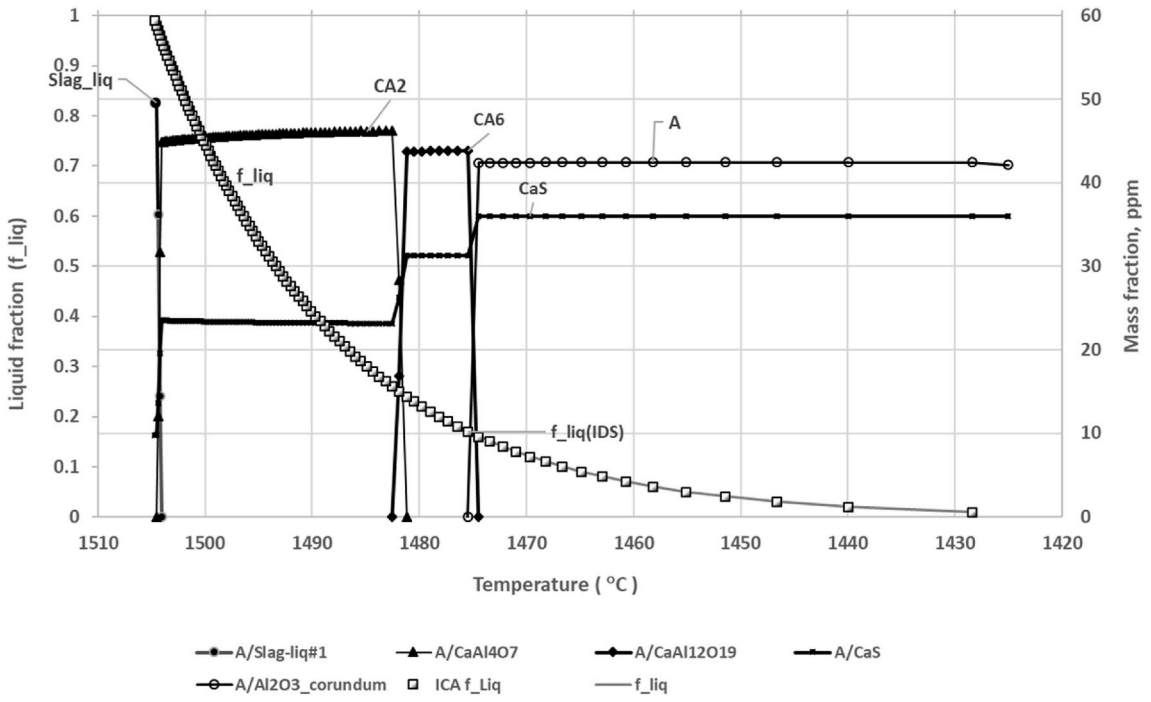

Fig. 5. Partial equilibria of oxide and sulphide inclusions in steel solidification with composition *C* 0.35 %, *Si* 0.25 % *S* 0.25 %, *O* 20 ppm, *Ca* 20 and *Al* 200 ppm. Liquid fraction (f_liq) adapted from Holappa et al. (2002) [28].

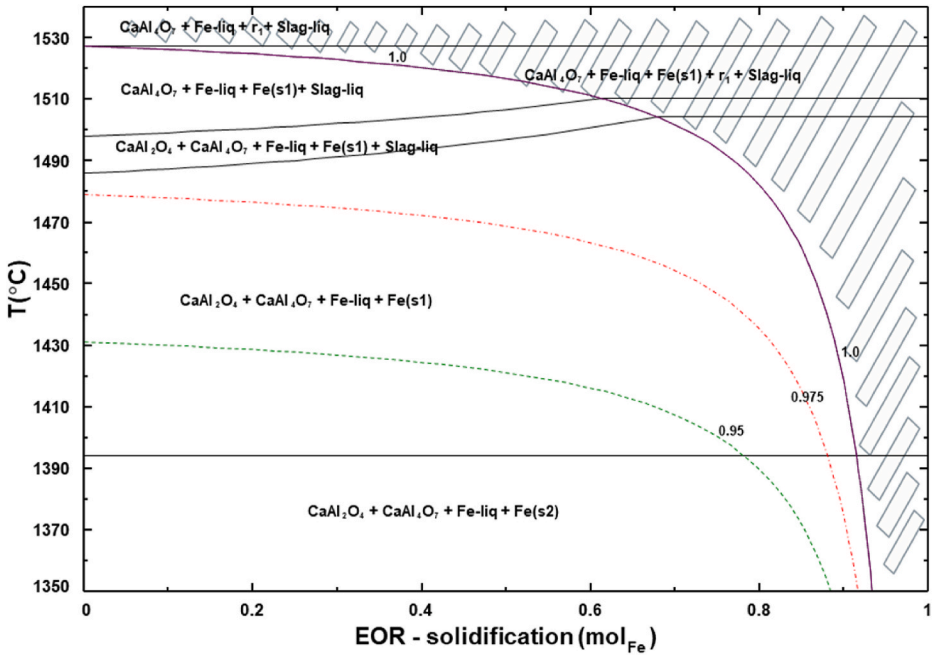

Fig. 6. T, ξ-phase diagram of the steel solidification system ($Fe-Al-Si-Ca-O_2-v_1$). Molar ratios O_2/Fe =7.06E-5, Al/Fe= 1.26E-4, Si/Fe=5.01e-3, Ca/Fe =2.82E-5. Solid lines indicate equilibrium phase boundaries. The striped area with stable r_1-phase exceeds the equilibrium limit of solid and liquid iron. The dotted and dash-dotted lines represent iso-activities of the virtual phase r_1. FactSage 7.3 FToxid database for pure oxide phases, CA2 included.

technique is affected by both the overall rate of CO_2 absorption and the solubility of sodium bicarbonate, which is the precipitating solid in the sorption system.

The solubility of $NaHCO_3$ increases with temperature. Knuutila et al. have recently performed vapour–liquid equilibrium (VLE) measurements of the carbon dioxide loaded sodium carbonate–water system in the temperature range 40–80 °C and for sodium carbonate concentrations 8–12 wt% [35]. Equation-of-state (VLE) calculations were also performed by using the Non-Random Two-Liquid model for electrolytes (e-NRTL). In Fig. 8 the results published by Knuutila et al. (40 and 60 °C) are compared with respective ChemSheet equilibrium calculations for temperatures 40–80 °C, with one result (40 °C) from the e-NRTL model. In ChemSheet, temperature-dependent Pitzer parameters are typically used from the concise database developed by Pajarre et al. [36]; in this case both models agree reasonably well with each other and with measurements.

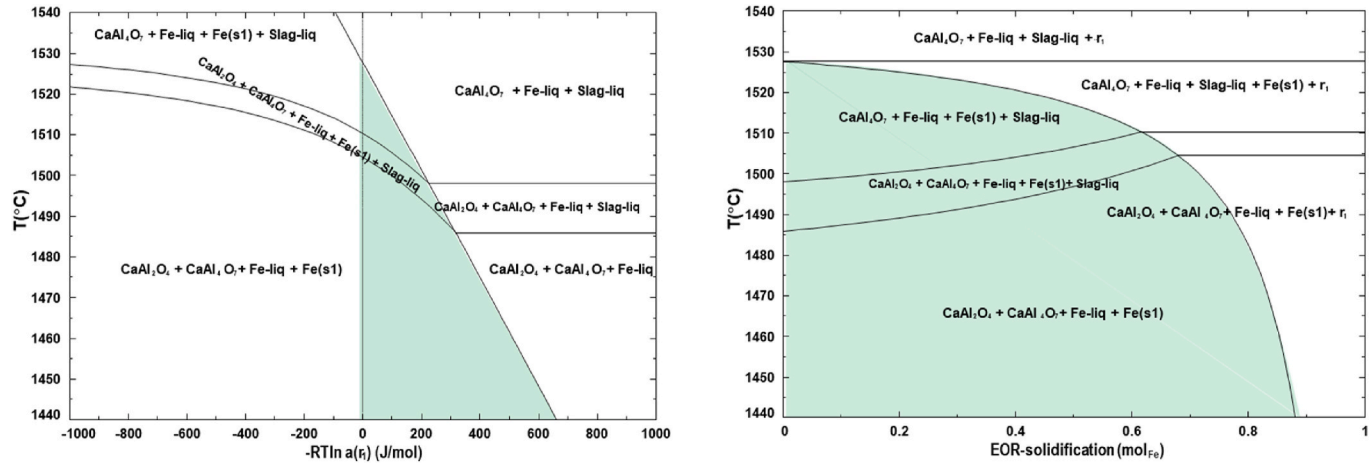

Fig. 7. T,ξ- phase diagram of the steel solidification system (right) and respective T,D-potential diagram (left). Molar ratios O_2/Fe =7.06E-5, Al/Fe= 1.26E-4, Si/Fe=5.01e-3, Ca/Fe =2.82E-5. FactSage 7.3 FToxid database for solid phases.

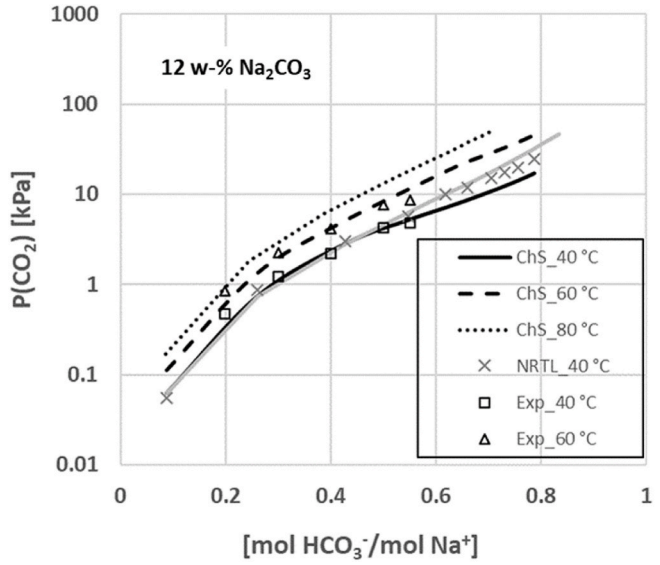

Fig. 8. The partial pressure of CO_2 as a function of Na_2CO_3 conversion to bicarbonate in 12 wt % Na_2CO_3 solution. The lines show ChemSheet equilibrium results, measured data and e-NRTL-model points are from Knuutila et al. (2010) [35]. The grey solid line refers to ChemSheet equilibrium calculation at 40 °C with no solid phases allowed, corresponding true VLE conditions.

A respective aqueous phase diagram for the equilibrium system is shown in Fig. 9 in terms of the partial pressure of CO_2 and Na_2CO_3 molality. In such a diagram, the temperature dependent solubility of $NaHCO_3$ becomes clearly visible and the iso-pH-lines (only shown for 32 °C) will serve as an additional guideline, e.g. when used to support practical purposes. The multicomponent diagram calculation may also comprise gaseous impurities (such as H_2S), the equilibrium distribution of which between gas and liquid may be read directly from the data at each point of the diagram.

To illustrate the usage of affinity- extent of reaction -diagrams for such aqueous systems the constraints were set for the absorption of CO_2 and precipitation of bicarbonate, as shown in Table 5.

In Fig. 10 (left) , the equilibrium diagram of $H_2O - Na_2CO_3 - CO_2$-N_2- system is presented using molalities (m) of CO_2 and Na_2CO_3 as axis variables. Then in Fig. 10 (right), the affinity of reaction r_2^+ has been used for the Y-axis, while the reaction r_1^+ is assumed to be in equilibrium ($H_2O - Na_2CO_3 - CO_2$- $N_2 - \nu_1 - \nu_2$ system). The effect of temperature on the solubility of sodium bicarbonate is shown equally when compared with Fig. 9. The affinity of $NaHCO_3$ precipitation is positive at 32 °C in the region where the molality of Na_2CO_3 exceeds 0.442 m while the same limit for the precipitation equilibrium at 60 °C is observed at 0.732 m. The zero phase fraction line crosses the zero affinity line at these points, equally recognised in the respective equilibrium diagram when following 1 m CO_2 dotted line in Fig. 10 (left).

In Fig. 11 the affinity of $NaHCO_3$ precipitation is assumed to be zero and the extent of reaction r_1^+ has been used for the x-axis variable instead. For the time being, FactSage only allows the use of positive integers as virtual constraints and thus the constraint of reaction 1 was actually set for all carbonaceous species in the aqueous solution as well as in condensed phases, i.e. regarding all these as products of constrained CO_2 absorption, yet in mutual equilibrium with each other. Then, the zero point for the EOR-x-axis must be set for the amount of constraint (r_1^+ phase) in the feed, while FactSage, of course performs the calculation using the total amount of this component. In Fig. 11 the amount of feed Na_2CO_3 is 0.3435 $m$and a system containing 0.4027 $m$of r_1^+ gives a condition of 0.283 m Na_2CO_3 and 0.226 m $NaHCO_3$ in the solution, corresponding to the condition in the experiment of Wylock et al. , performed at 293 K, 1 atm.

The T,ξ-diagram maps the reaction process, also indicating the conditions for $NaHCO_3$-precipitation and the equilibrium limit for CO_2 absorption. As the work of Wylock et al. was entirely based on concentration variables, their reported pH-values were adjusted to correspond to the respective hydrogen ion activities to compare with the iso-pH-lines in the FactSage diagram at 293 K, shown on this isotherm. Yet one must keep in mind that no kinetic rate parameters are involved and thus while the pH values for the initial condition and the final equilibrium at each temperature are well defined, the intermediate region is subject to the assumption of local chemical equilibrium, while the EOR-constraint, by necessity, does not include any mechanistic assumptions. Thus, the iso-pH lines in the intermediate region remain somewhat approximate. The graphs indicate that the EOR- diagram method allows for a robust approach to foresee expected reaction conditions within a relevant pH range, including pH-dependent formation of solids, which often is omitted when using kinetic modelling procedures (e.g. Wylock et al., 2008).

Fig. 12 finally shows the overlapping (superimposed) diagrams for the non-constrained equilibrium system and for the respective constrained system in which both affinity of CO_2 absorption and $NaHCO_3$ precipitation are assumed to be zero. The overlap is best visible in the slightly deflected iso-pH curves, while the zero phase fraction-lines fully coincide, as the equilibrium conditions are then restored within the constraint method.

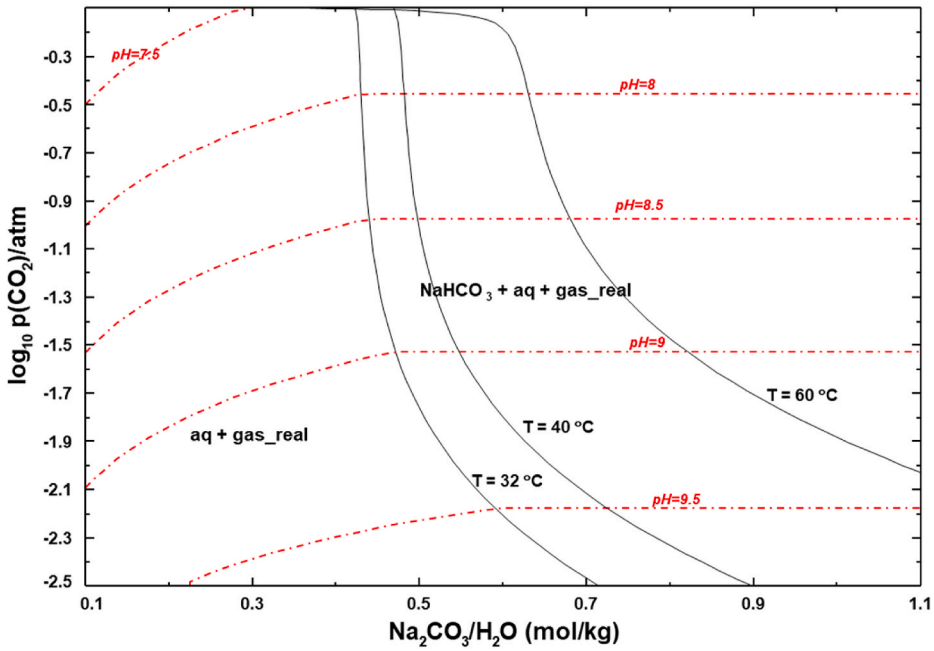

Fig. 9. Aqueous phase diagram for the $H_2O-Na_2CO_3$-N_2 –system. N_2 /H_2O (mol/kg)=1.2; 32-60 °C, 1 atm. Superimposition of three temperatures shows the increasing solubility of $NaHCO_3$ with increase of temperature. Iso-pH curves shown merely for T= 32 °C.

Table 5
Extended matrix for the aqueous carbon dioxide–sodium carbonate absorption system. Constraints set for the reactions $CO_2(g) \rightarrow CO_2(aq)$; (r_1^+, r_1^-) and $Na^+ + HCO_3^- \rightarrow NaHCO_3$; (r_2^+, r_2^-)

N	O	C	H	Na	EA	ν_1	ν_2	
2	0	0	0	0	0	0	0	$N_2(g)$
0	2	0	0	0	0	0	0	$O_2(g)$
0	2	1	0	0	0	1	0	$CO_2(g)$
0	1	0	2	0	0	0	0	$H_2O(g)$
0	1	0	2	0	0	0	0	H_2O
0	0	0	1	0	-1	0	0	H^+
0	1	0	1	0	1	0	0	OH^-
0	2	1	0	0	0	0	0	$CO_2(aq)$
0	3	1	1	0	1	0	0	HCO_3^-
0	3	1	0	0	2	0	0	CO_3^{2-}
0	0	0	0	1	-1	0	0	Na^+
0	3	1	0	2	0	0	0	$Na2CO_3$
0	1	0	1	1	0	0	0	NaOH
0	3	1	1	1	0	0	1	$NaHCO_3$
0	0	0	0	0	0	1	0	r_1^+
0	0	0	0	0	0	-1	0	r_1^-
0	0	0	0	0	0	0	1	r_2^+
0	0	0	0	0	0	0	-1	r_2^-

5. Discussion

The addition of the virtual component brings an additional potential that represents the driving force of an internal process (affinity of a chemical reaction), while the respective virtual constituent as an axis variable provides the option to map the phase transformations as the sections of a phase diagram in terms of the extent of such internal process. This was shown in Figs. 2 and 6 where limiting temperature ranges of oxyhydrate and oxysulphate and CA-inclusions remain visible as only gradual transformation to end products ($TiO_2(Ru)$ and $Fe-Bcc$) is allowed. The diagram may then include superimposed phase compositions from any viable kinetic model and/or experimentally determined reaction path as shown in Fig. 2 or, respectively, if the data from Fig. 5 was positioned in Fig. 6 by converting the f_{liq} -record to a $T(\xi)$- solidification curve, giving a kind of an isothermal transformation (TTT) diagram, represented in terms of the chosen extent of reaction without explicit time dependence. For such screening, of course the assumptions made for local equilibria could (and should) then be verified against experimental observation.

The use of the driving force as an axis gives an option to study conditions far from equilibria, provided that the assumptions of the appropriate (established) local equilibria in the multicomponent system are valid. It also allows the use of present-day phase diagram software to compare the stabilities of stoichiometrically equivalent compounds, the Gibbs energy of which may yet depend on crystal structure or, e.g. size of particulates.

As for aqueous solutions it seems that the driving force- extent of reaction-screening for phase changes also gives viable possibilities. While it is well-known that the Gibbs energy data for aqueous systems (e.g. the enthalpies of formation of the precipitating salts) is often inaccurate, the aqueous processes also frequently appear in non-equilibrium states that involve slow reaction kinetics or in metastable conditions, for which, however, intensive properties such as temperature, pH and redox potential (Eh) as well as molar concentrations of given ionic species can be measured with relative ease and with reasonable accuracy. It may be anticipated that computational studies of the ‘freezing-in-conditions’ for these systems will have practical significance both in model-based design of experiments as well as in interpreting measured results.

As stated above, setting constraints for the advancement of chemical reactions should be generally applicable for thermodynamic and phase diagram software which makes use of the Lagrange method in Gibbs energy minimization. The strictly necessary condition is for the user to be able to specify the new components to the stoichiometry of relevant species as is done by the new columns labeled ν_1 and ν_2 in Tables 2 and 5. These new components should have a zero molar mass so that they do not contribute to the molar mass of the relevant species (see Supplementary Appendix). If definition of zero molar mass is not possible, the inputs should be specified in molar units in all the calculations. The added virtual phases ($r_i^{\pm}$) with a zero enthalpy, entropy and heat

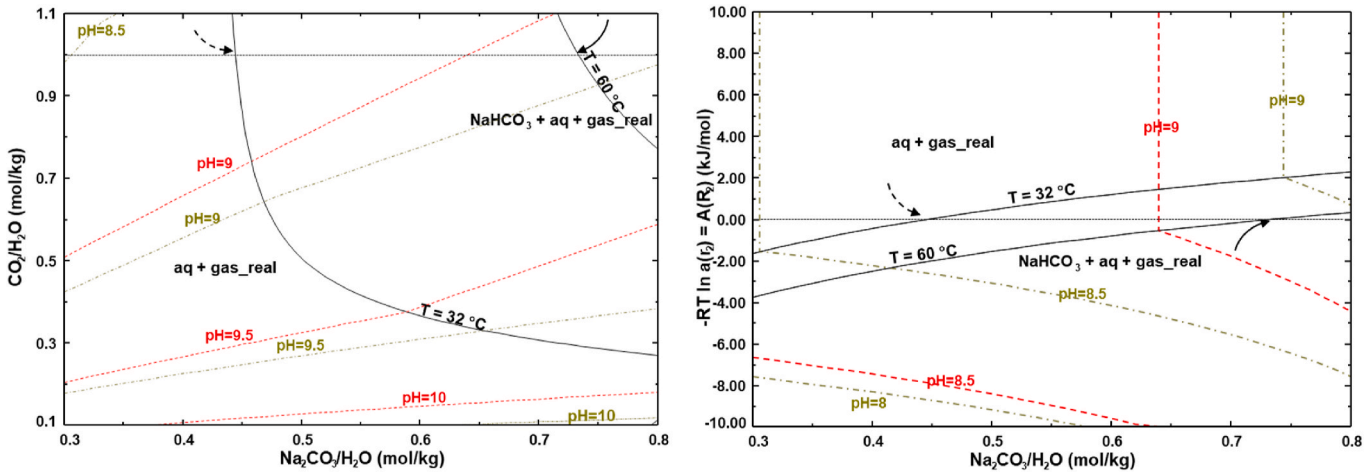

Fig. 10. Aqueous phase diagram for the $H_2O - Na_2CO_3 - CO_2 - N_2$ –equilibrium system (left) compared with the potential diagram where the affinity of CO_2 absorption is assumed to be zero and *Y*-axis shows the driving force of $NaHCO_3$precipitation (right). N_2 /H_2O (mol/kg)=4; pH colour code: olive dash-dot – 32 °C; red dashed – 60 °C. The corresponding equilibrium points at 1.0 mol CO_2 / kg H_2O are marked with dashed (32 °C) and solid (60 °C) arrows. (For interpretation of the references to colour in this figure legend, the reader is referred to the Web version of this article.)

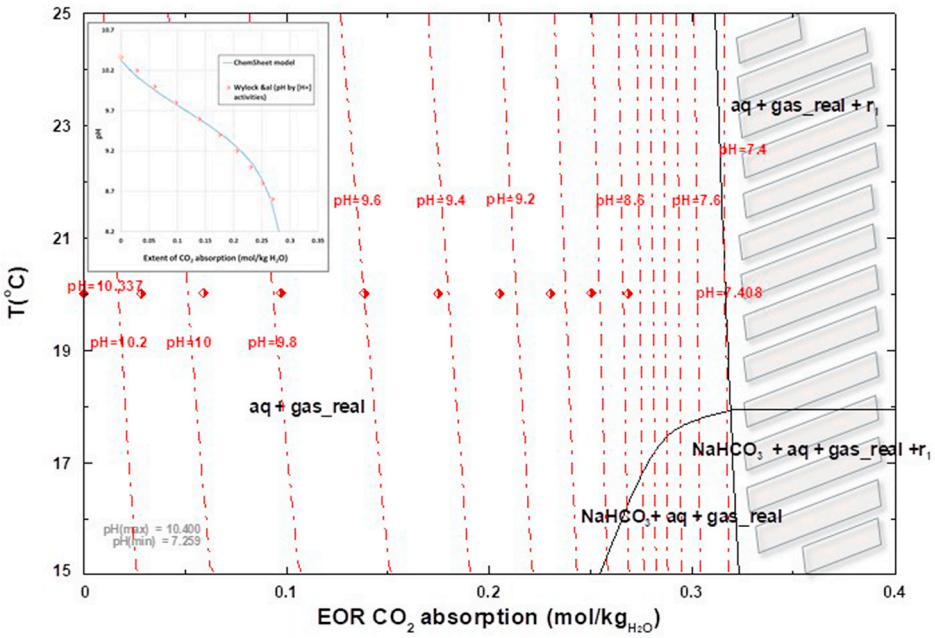

Fig. 11. Temperature – extent of reaction diagram for the $H_2O - Na_2CO_3 - CO_2 - N_2 - \nu_1 - \nu_2$ -system at 1 atm Na_2CO_3 0.3425 *m*; r_1^+ 0.4027 *m*; CO_2 1.0 *m*. Affinity of $NaHCO_3$ precipitation is set to zero. Extent of the absorption reaction is assumed to follow the constraint set for carbonaceous species in the liquid and solid phases. Experimental points of Wylock et al. [33] as adjusted to the FactSage activity scale shown at the 'isotherm' of 293 K, each value shows measured pH of the nearest calculated iso-pH line at given EOR (end points with their pH-values are shown separately). The insert shows the respective ChemSheet model result at 20 °C. The striped area is beyond the saturation limit of CO_2-absorption.

capacity and the stated stoichiometries in Tables 2 and 5, are required for Figures like those in 2, 6,7 and 11 where one wants to explicitly show the area corresponding to the extent of reaction that would be beyond the equilibrium considering the defined initial state. They are also used as an practical input variable (for keeping all other inputs definitions equal while changing the extent of reaction) and further used in Figs. 5 and 7 where their chemical potential ($RT \ln a_{r_1^\pm}$) is applied for accessing the corresponding reaction affinity as the x-axis variable. The corresponding affinity would be defined in the system also without these virtual phases, but one should then make sure that this property can be used as the axis component when producing the diagram.

The received information, though often approximate, includes data for a wide operational range and inherently includes phase change and equilibrium conditions. The thermodynamics-based diagrams provide a practicable technique to approximate reaction conditions when/if lacking kinetic data, also being related with techniques used, e.g. for Scheil solidification and paraequilibrium studies. While the use of D, ξ-diagrams is by necessity restricted with the limited number of assumptions, the respective CFE approach can of course be further developed to kinetic-thermodynamic process models, which then include the necessary mechanistic assumptions as well as time-dependent rate parameters [5,16,19].

6. Conclusions

The driving force (affinity, *D*) and extent of reaction (EOR, ξ) were used as axis variables to produce phase diagrams for non-equilibrium conditions by using the Calphad method. The particular focus was in studying the thermodynamic validity of the suggested technique, which is pursued to be consistent with the methodology that is used for conventional equilibrium phase diagrams. Three examples for various thermochemical systems included a solid state reaction, melt solidification and an aqueous sorption-precipitation system.

The results indicate that the proposed affinity-EOR-diagrams are

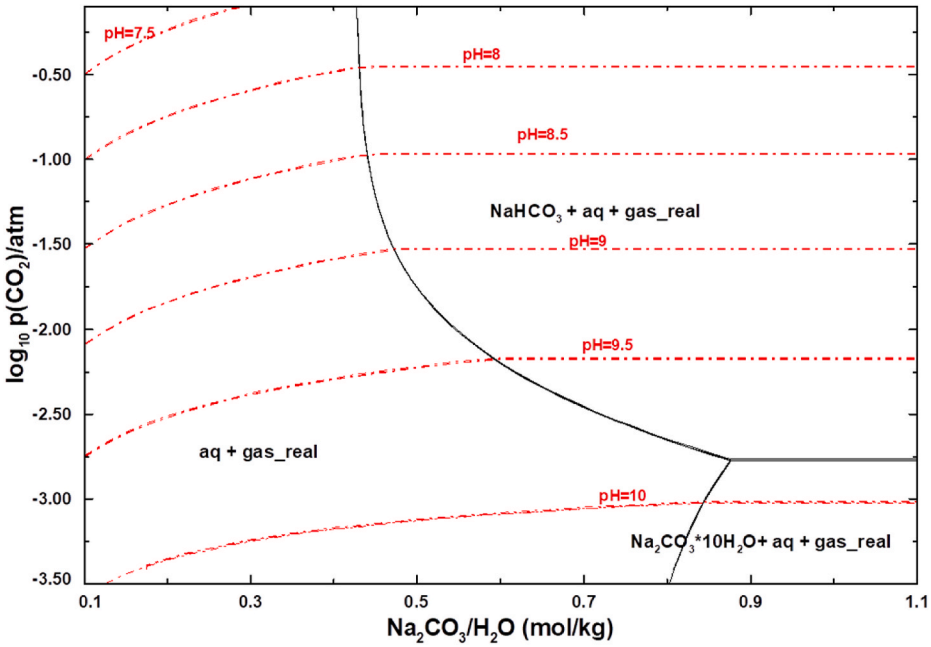

Fig. 12. Equilibrium phase diagram for the $H_2O - Na_2CO_3 - CO_2$- N_2- system N_2 /H_2O (mol/kg)=0.163; 32 °C, 1 atm. The figure shows overlapping (superimposed) diagrams for the non-constrained equilibrium system and for the respective constrained system in which both affinity of CO_2 absorption and $NaHCO_3$ precipitation are assumed to be zero. The overlap is best visible in the slightly deflected iso-pH curves.

generically applicable for various Calphadian problems. The thermodynamics-based approach can be used for non-equilibrium studies when measured kinetic data is not available and gives a method that can be used with common phase diagram software to support practical purposes, say in design of model-based experimental work. The new method can be applied for 'mapping' reaction conditions in terms of thermodynamic potentials and concentration variables. The technique also provides an additional degree of freedom when studying stoichiometrically identical (isomeric) transformations and surface energy effects. The inherent local equilibrium assumption is useful for following side reactions in a multicomponent phase transformation system with one or two main reactions, giving ample data for such reaction systems, e.g. within a wide temperature and/or pH range.

Final technical note: The technique is so far somewhat hampered by limited compatibility with the present software available to the authors. Thus, the results of ChemSheet models and T, ξ- and T, D -diagrams should not be compared on a one-to-one basis, as somewhat simplified data input files had to be used to produce the diagrams in FactSage Versions 7.2 and 7.3. The inconsistency affects both the *Fe*-solidification system and the aqueous sorption model and is due to the fact that the large data files applied in ChemSheet/ChemApp CFE models were not compatible with present FactSage software. Thus, some minor inconsistencies with the phase description and phase transformation conditions appear, which do not, however, affect the inferences concerning the methodology.

Funding

This work was funded by Business Finland, grant nr 755/31/2018.

Data availability statement

Data used in the titania calcination and CO_2 absorption examples are given in the supporting material and in Ref. [35]. For the steel solidification case parameters from FactSage database can be used.

Declaration of competing interest

The authors declare that they have no known competing financial interests or personal relationships that could have appeared to influence the work reported in this paper.

Appendix A. Supplementary data

Supplementary data to this article can be found online at https://doi.org/10.1016/j.calphad.2021.102290.

References

[1] M. Hillert, Phase Equilibria, Phase Diagrams and Phase Transformations: Their Thermodynamic Basis, second ed., Cambridge University Press, Cambridge, 2007.
[2] Z.-K. Liu, Y. Wang, Computational Thermodynamics of Materials, Cambridge University Press, Cambridge, United Kingdom, 2016, https://doi.org/10.1017/cbo9781139018265.
[3] T. De Donder, P. Van Rysselberghe, Thermodynamic Theory of Affinity, Stanford University Press, Stanford, 1936.
[4] P. Koukkari, R. Pajarre, Calculation of constrained equilibria by Gibbs energy minimization, Calphad Comput, Coupling Phase Diagrams Thermochem. 30 (2006) 18–26, https://doi.org/10.1016/j.calphad.2005.11.007.
[5] R. Pajarre, P. Koukkari, P. Kangas, Constrained and extended free energy minimisation for modelling of processes and materials, Chem. Eng. Sci. 146 (2016) 244–258, https://doi.org/10.1016/j.ces.2016.02.033.
[6] Z.K. Liu, Computational thermodynamics and its applications, Acta Mater. 200 (2020) 745–792, https://doi.org/10.1016/j.actamat.2020.08.008.
[7] A.D. Pelton, P. Koukkari, R. Pajarre, G. Eriksson, Para-equilibrium phase diagrams, J. Chem. Thermodyn. 72 (2014) 16–22, https://doi.org/10.1016/j.jct.2013.12.023.
[8] C.W. Bale, P. Chartrand, S.A. Degterov, G. Eriksson, K. Hack, R. Ben Mahfoud, J. Melançon, A.D. Pelton, S. Petersen, FactSage thermochemical software and databases, Calphad 26 (2002) 189–228, https://doi.org/10.1016/S0364-5916(02)00035-4.
[9] P. Koukkari, K. Penttilä, M. Keegel, Coupled thermodynamic and kinetic models for high-temperature processes, in: Proc. 10th Int. IUPAC Conf. High Temp. Mater. Chem, Forscungszentrum Jülich, 2000, pp. 253–256.
[10] P. Koukkari, R. Pajarre, K. Hack, Setting kinetic controls for complex equilibrium calculations, Zeitschrift Fuer Met. Res. Adv. Tech. 92 (2001) 1151–1157.
[11] G. Eriksson, K. Hack, S. Petersen, No Title, in: Werkstoffswoche '96, Symp. 8 Simul. Model. Informationsysteme, vol. 47, DGM Informationsgesellschaft, mbH, Frankfurt, 1997, ISBN 3-88355-236-4, 1997.
[12] P.R. Dumont, G. Belanger, Steady-state study of a titanium dioxide rotary kiln, Lnd. Eng. Chem. Process Des. Dev. (1978) 107–114.

[13] M. Ketonen, K. Penttilä, P. Koukkari, Simulation studies of a calcination kiln process, in: ECC 1997, Eur. Control Conf., 1997, pp. 723–729.
[14] T. Ginsberg, M. Modigell, Dynamic modelling of a rotary kiln for calcination of titanium dioxide white pigment, Comput. Chem. Eng. 35 (2011) 2437–2446, https://doi.org/10.1016/j.compchemeng.2011.03.029.
[15] P. Koukkari, R. Pajarre, Introducing mechanistic kinetics to the Lagrangian Gibbs energy calculation, Comput. Chem. Eng. 30 (2006) 1189–1196, https://doi.org/10.1016/j.compchemeng.2006.03.001.
[16] P. Koukkari, R. Pajarre, K. Hack, Constrained Gibbs energy minimisation, Int. J. Mater. Res. 98 (2007) 926–934, https://doi.org/10.3139/146.101550.
[17] P. Koukkari, R. Pajarre, P. Blomberg, Reaction rates as virtual constraints in Gibbs energy minimization, Pure Appl. Chem. 83 (2011) 1063–1074, https://doi.org/10.1351/PAC-CON-10-09-09.
[18] P.B.A. Blomberg, P.S. Koukkari, A systematic method to create reaction constraints for stoichiometric matrices, Comput. Chem. Eng. 35 (2011) 1238–1250, https://doi.org/10.1016/j.compchemeng.2010.07.024.
[19] R. Pajarre, Modelling of Chemical Processes and Materials by Free Energy Minimization, Doctoral thesis, Aalto University, 2016, ISBN 978-952-60-7154-1.
[20] P. Koukkari, E. Paiva, Mechanistic and constrained thermochemical modelling in chemical reactor engineering: Ti(IV) chloride oxidation revisited, Chem. Eng. Sci. 179 (2018) 227–242, https://doi.org/10.1016/j.ces.2018.01.016.
[21] P. Koukkari, R. Pajarre, P. Kangas, Thermodynamic affinity in constrained free energy systems, Monatshefte Für Chemie - Chem. Mon. 149 (2018) 381–394.
[22] K.J.D. Mackenzie, The calcination of titania V. -Kinetics and mechanism. Of the anatase-rutile transformation in the presence of additives, Trans. J. Br. Ceram. Soc. 74 (1975) 77–84.
[23] G. Mauer, A. Guignard, R. Vaßen, Plasma spraying of efficient photoactive TiO2 coatings, Surf. Coating. Technol. 220 (2013) 40–43, https://doi.org/10.1016/j.surfcoat.2012.08.042.
[24] M. Lind, Mechanism and Kinetics of Transformation of Alumina Inclusions in Steel by Calsium Treatment, Doctoral Thesis, Helsinki University of Technology, Edita, 2006, ISBN 951-22-8252-6.
[25] L. Holappa, M. Hämäläinen, M. Liukkonen, M. Lind, Thermodynamic examination of inclusion modification and precipitation from calcium treatment to solidified steel, Ironmak. Steelmak. 30 (2003) 111–115, https://doi.org/10.1179/030192303225001748.
[26] J. Miettinen, Calculation of solidification-related thermophysical properties for steels, Metall. Mater. Trans. B Process Metall. Mater. Process. Sci. 28 (1997) 281–297, https://doi.org/10.1007/s11663-997-0095-2.
[27] J. Miettinen, S. Louhenkilpi, H. Kytönen, J. Laine, IDS: thermodynamic-kinetic-empirical tool for modelling of solidification, microstructure and material properties, Math. Comput. Simulat. 80 (2010) 1536–1550, https://doi.org/10.1016/j.matcom.2009.11.002.
[28] L. Holappa, M. Hämäläinen, M. Liukkonen, M. Lind, Thermodynamic examination on inclusion modification and precipitation from calcium treatment to solidified steel, in: 6th Int.Conf.on Clean Steel Balatonfured, 2002. Hungary, 10-12 June 2002.
[29] K. Hack (Ed.), The SGTE Casebook, second ed., Woodhead Publishing Limited, Cambridge, United Kingdom, 2008.
[30] A.D. Pelton, G. Eriksson, K. Hack, C.W. Bale, Thermodynamic calculation of aqueous phase diagrams, Monatshefte Für Chemie - Chem. Mon. 149 (2018) 395–409, https://doi.org/10.1007/s00706-017-2094-6.
[31] A.H.G. Cents, D.W.F. Brilman, G.F. Versteeg, CO2 absorption in carbonate/bicarbonate solutions: the Danckwerts-criterion revisited, Chem. Eng. Sci. 60 (2005) 5830–5835, https://doi.org/10.1016/j.ces.2005.05.020.
[32] U.K. Ghosh, S.E. Kentish, G.W. Stevens, Absorption of carbon dioxide into aqueous potassium carbonate promoted by boric acid, Energy Procedia 1 (2009) 1075–1081, https://doi.org/10.1016/j.egypro.2009.01.142.
[33] C.E. Wylock, P. Colinet, T. Cartage, B. Haut, Coupling between mass transfer and chemical reactions during the absorption of CO2 in a NaHCO3-Na2CO3 brine: experimental and theoretical study, Int. J. Chem. React. Eng. 6 (2008) 1–20, https://doi.org/10.2202/1542-6580.1502.
[34] M. Wallin, S. Olausson, Simultaneous absorption of H2S and CO2 into a solution of sodium carbonate, Chem. Eng. Commun. 123 (1993) 43–59.
[35] H. Knuutila, E.T. Hessen, I. Kim, T. Haug-Warberg, H.F. Svendsen, Vapor-liquid equilibrium in the sodium carbonate-sodium bicarbonate-water-CO2-system, Chem. Eng. Sci. 65 (2010) 2218–2226, https://doi.org/10.1016/j.ces.2009.12.024.
[36] R. Pajarre, P. Koukkari, P. Kangas, Industrial and Mine Water Chemistry: Advanced Aqueous Database for Modelling Industrial Processes, VTT Technology Series T321, Espoo, 2018.
[37] G. Eriksson, S. Petersen, Programmer's Manual Edition 4.00 for ChemApp Versions 2.0.2 through 6.4.0, 2016. Chapter 11: Thermochemical Data-files - Structure and Handling, https://gtt-technologies.de/software/chemapp/documentation/online-manual/.

Nomenclature

A: Frequency factor of chemical reaction
A_r*:* Affinity of chemical reaction *r*
c_{kj}*:* element the stoichiometric conservation matrix *C* of the thermodynamic system
D, D_r*:* Driving force of an internal process, equals affinity of chemical reaction
E_a*:* Activation energy of a chemical reaction
G: Gibbs energy
k: rate constant of a chemical reaction
L: Lagrangian objective function for Gibbs free energy minimization
m: symbol of the molality unit for an aqueous solute species (mol/kg H_2O)
n_k*:* molar amount of phase constituent (species) *k*
N_j*:* molar amount of independent system component *j*
N: number of constituents in the Gibbs'ian system
NC: number of components in the Gibbs'ian system
NR: number of chemical reactions
P: Pressure
R: Gas constant
R_i*:* Abbreviation for a chemical reaction ($i = 1, 2$)
r_i, $r_i^{\pm}$*:* Symbol for a virtual (reaction) phase in the conservation matrix ($i = 1, 2$ used for reactions), superscripts indicate forward or reverse reaction
t, t_r*:* time, residence time of a reaction
T: Temperature
S: Entropy
U: Internal energy
V: Volume
v_j*:* Symbol for a virtual component in the conservation matrix ($j = 1, 2$used for reactions)
X: symbol used for extensive conjugate variables
λ*:* Lagrange undetermined multiplier
μ_k*:* Chemical potential of constituent *k*
μ_j*:* Chemical potential of component *j*
$\mu^0_{r_i^{\pm}}$*:* Standard chemical potential of virtual phase $r_i^{\pm}$
ξ*:* extent of a chemical reaction